

M^{II} (M = Mn, Fe, Co, Ni and Cu) complexes with a chromone-derived neutral ligand: synthesis, structural characterization, photocatalytic and mycobacterial activity studies

Mariana Letícia Munin Camargo,^a Cristiane Storck Schwalm,^a Tanize Bortolotto,^b Natália de Freitas Daudt,^c Grazielle Guidolin Rossi,^d Marli Matiko Anraku de Campos,^d Kaique Alexandre D’Oliveira,^e Alexandre Cuin,^e * and Vânia Denise Schwade^{a,b} *

^a Faculty of Exact Sciences and Technology, Federal University of Grande Dourados, Rod. Dourados/Itahum, Km 12, 79804-970, Dourados, MS, Brazil

^b Department of Chemistry, Natural and Exact Sciences Centre, Federal University of Santa Maria, Av. Roraima, n.1000, 97105-900, Santa Maria, RS, Brazil

^c Department of Mechanical Engineering, Federal University of Santa Maria, Av. Roraima, n.1000, 97105-900, Santa Maria, RS, Brazil

^d Department of Clinical and Toxicological Analysis, Federal University of Santa Maria, Av. Roraima, n.1000, 97105-900, Santa Maria, RS, Brazil

^e LQBin – Laboratory of BioInorganic Chemistry, Chemistry Department, Exact Science Institute, Federal University of Juiz de Fora, Juiz de Fora, MG, Brazil

Corresponding authors

* V. D. Schwade: vania.schwade@uol.com.br and A. Cuin: alexandre.cuin@ufjf.edu.br

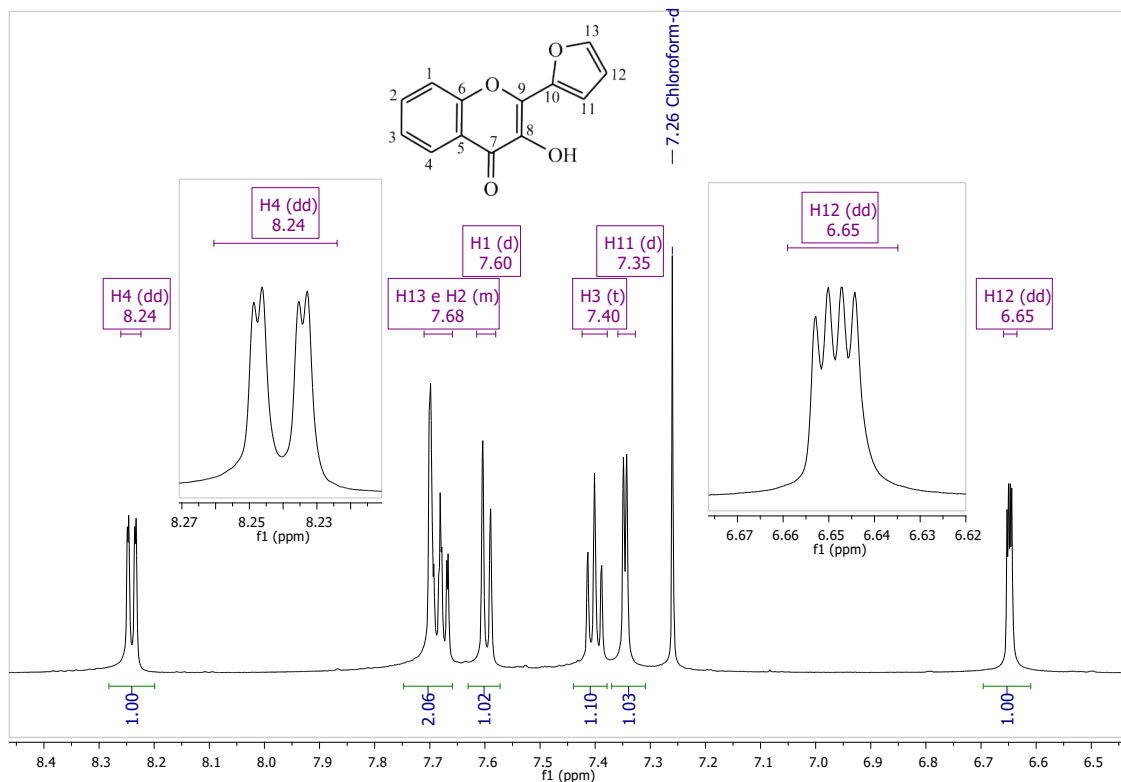


Fig. S1. ^1H NMR spectrum (600.1 MHz, CDCl_3) of 2-furyl-3-hydroxychromone.

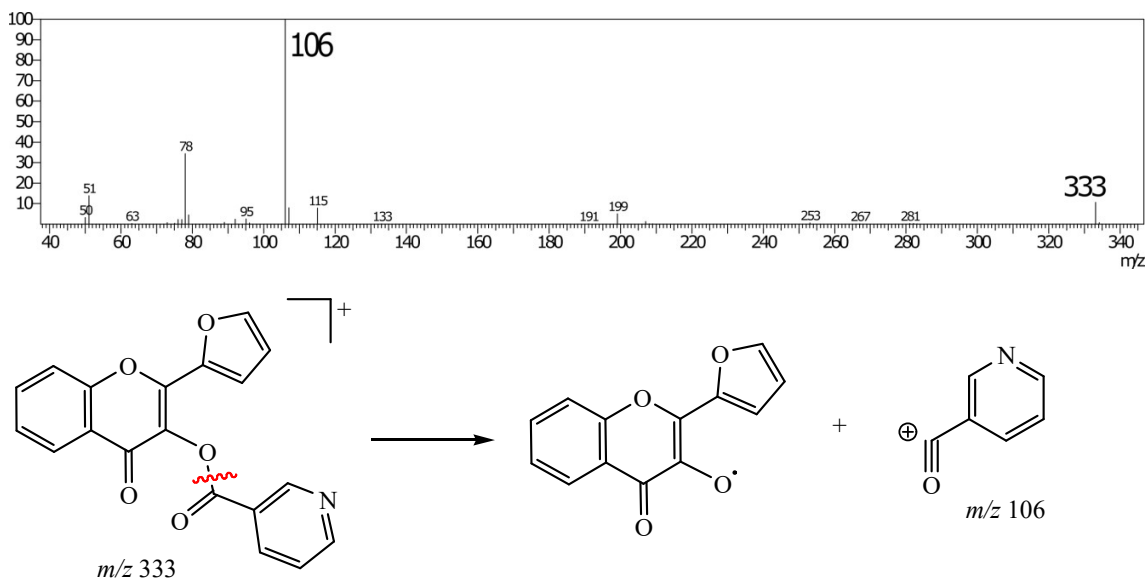


Fig. S2. Mass spectrum of the 2-furyl-3-hydroxychromone-derived ligand and its fragmentation. The compound was dissolved in ethyl acetate for the analysis.

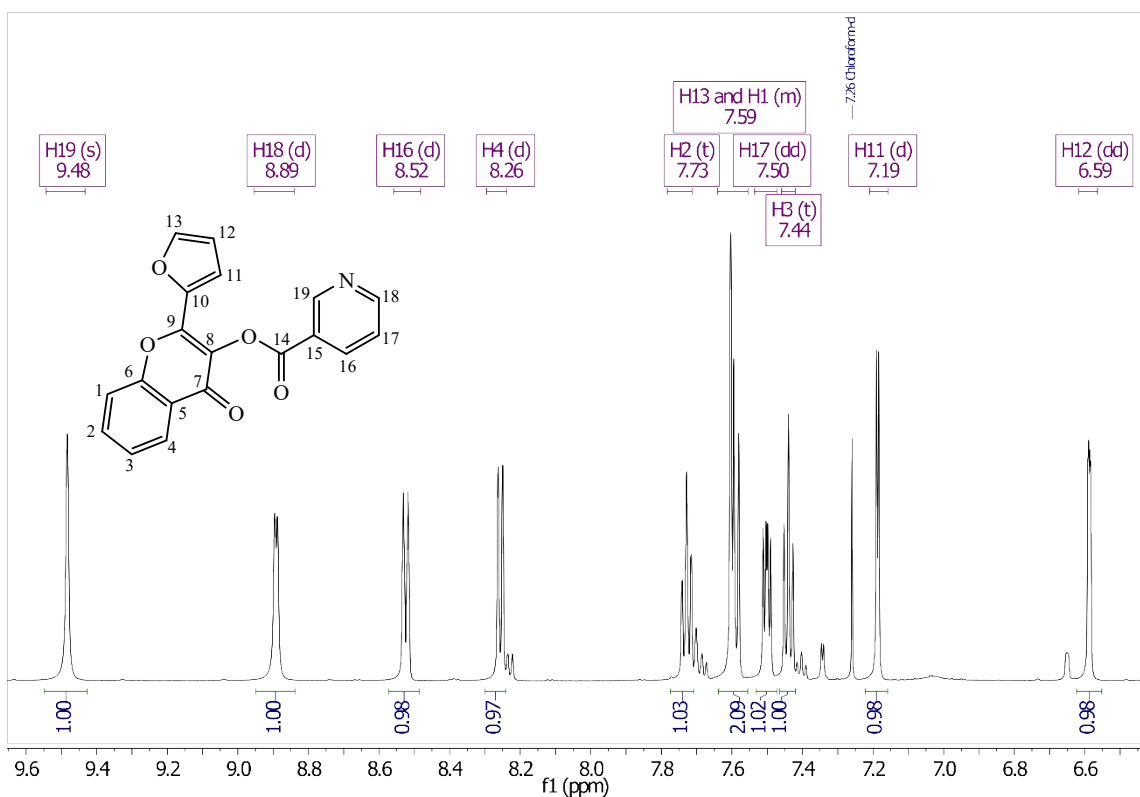


Fig. S3. ¹H NMR spectrum (600.1 MHz, CDCl₃) of the 2-furyl-3-hydroxychromone-derived ligand, L.

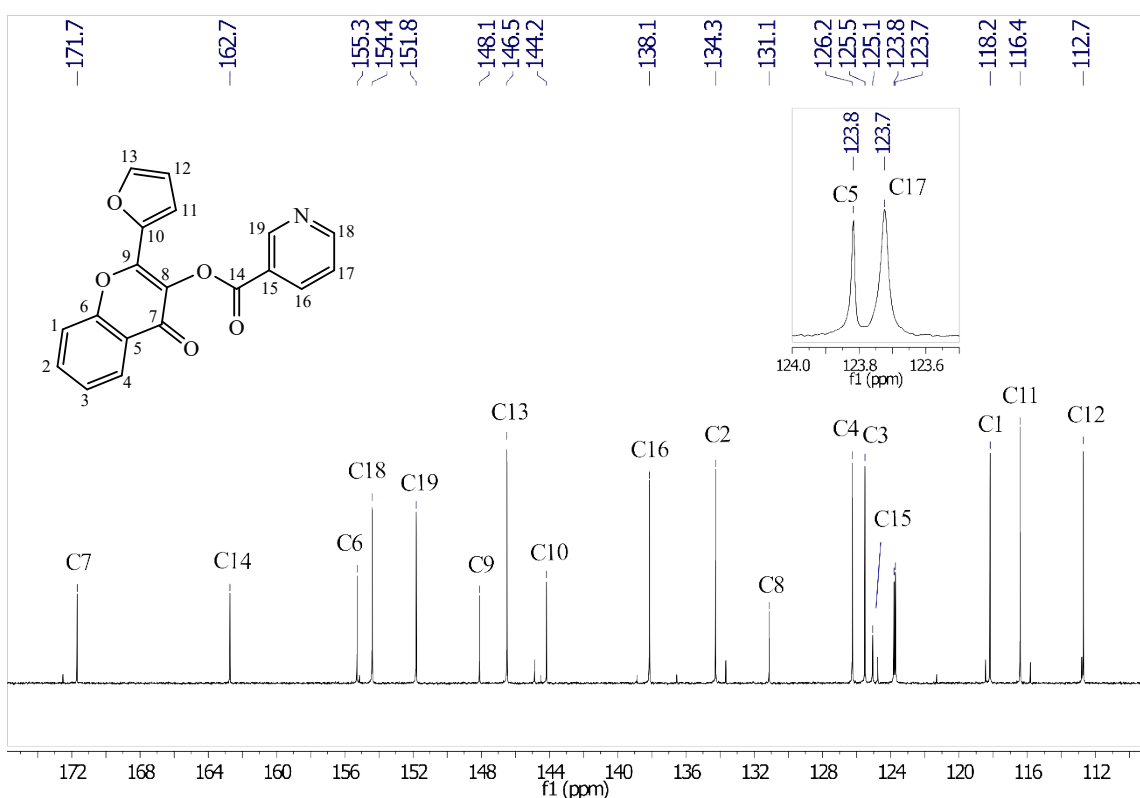


Fig. S4. ¹³C NMR spectrum (150.9 MHz, CDCl₃) of L.

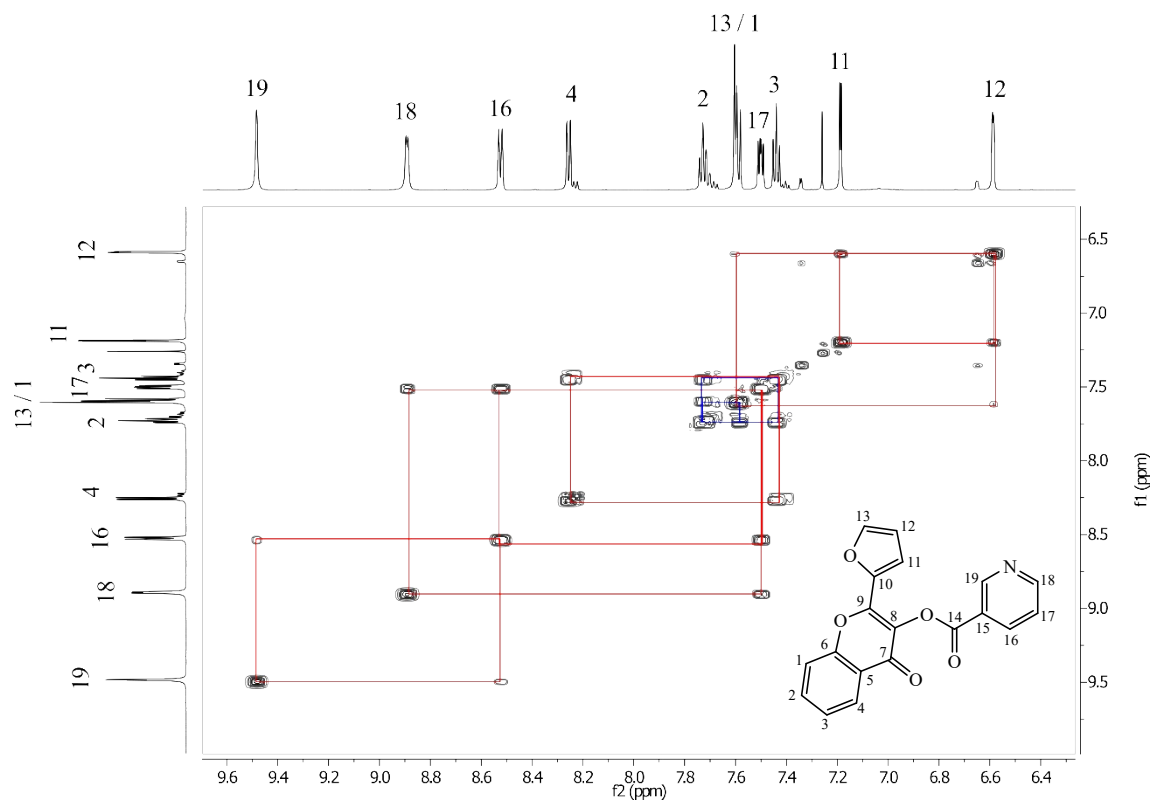


Fig. S5. COSY spectrum (CDCl_3) of **L**.

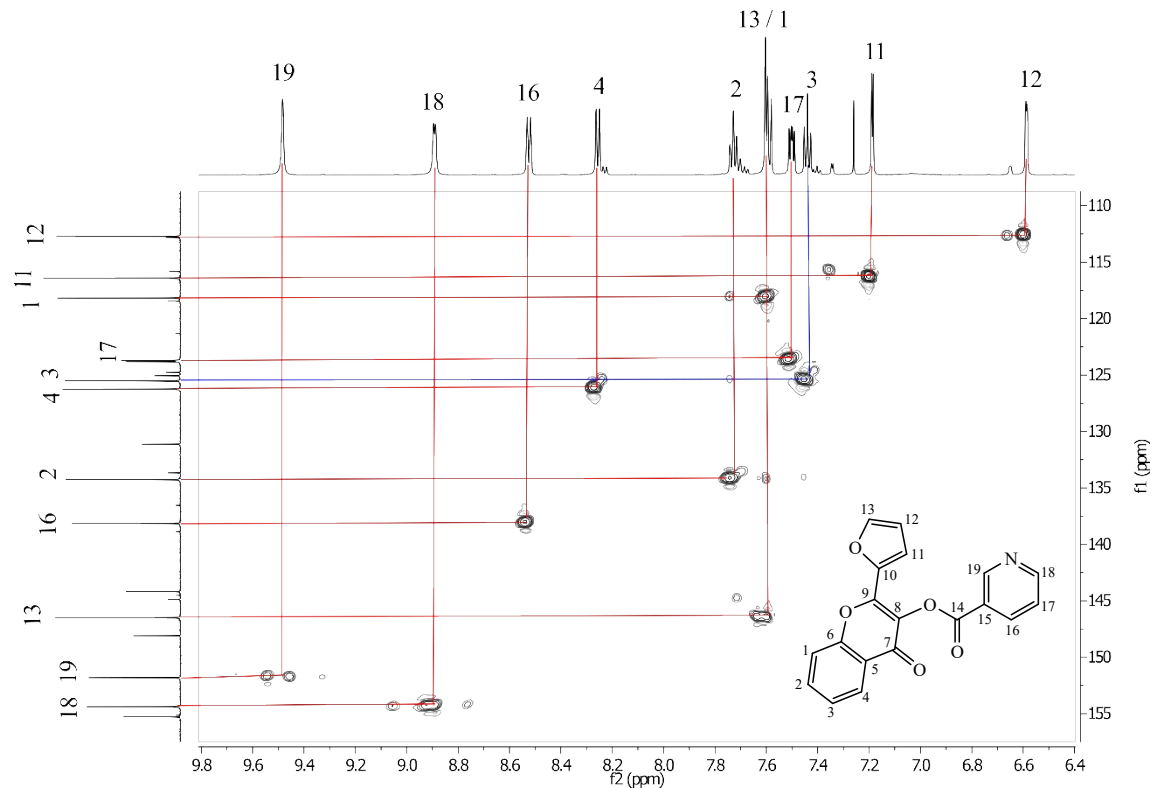


Fig. S6. HSQC spectrum (CDCl_3) of **L**.

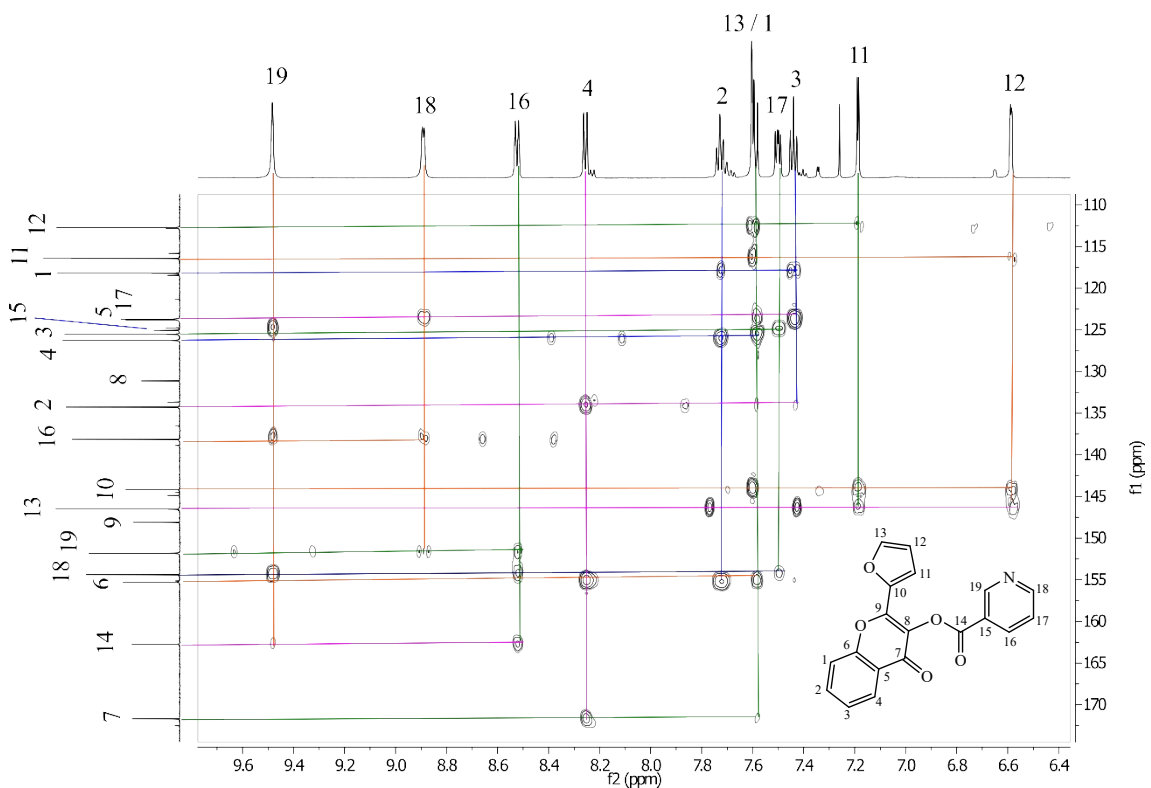
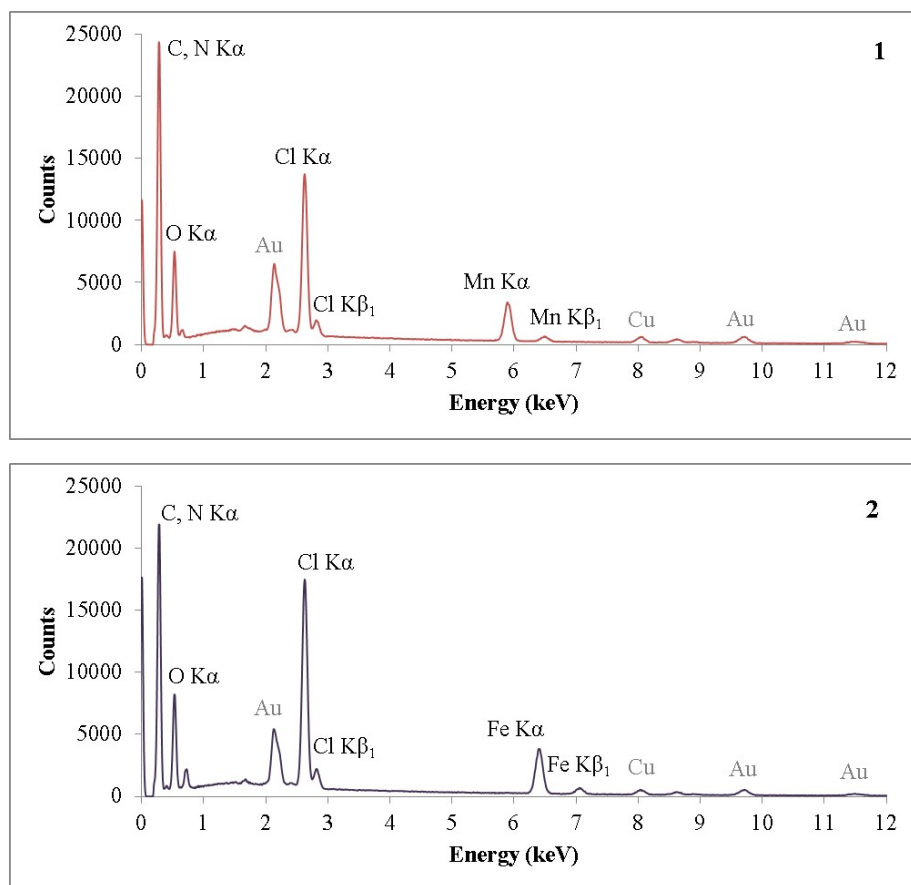


Fig. S7. HMBC spectrum (CDCl_3) of L.



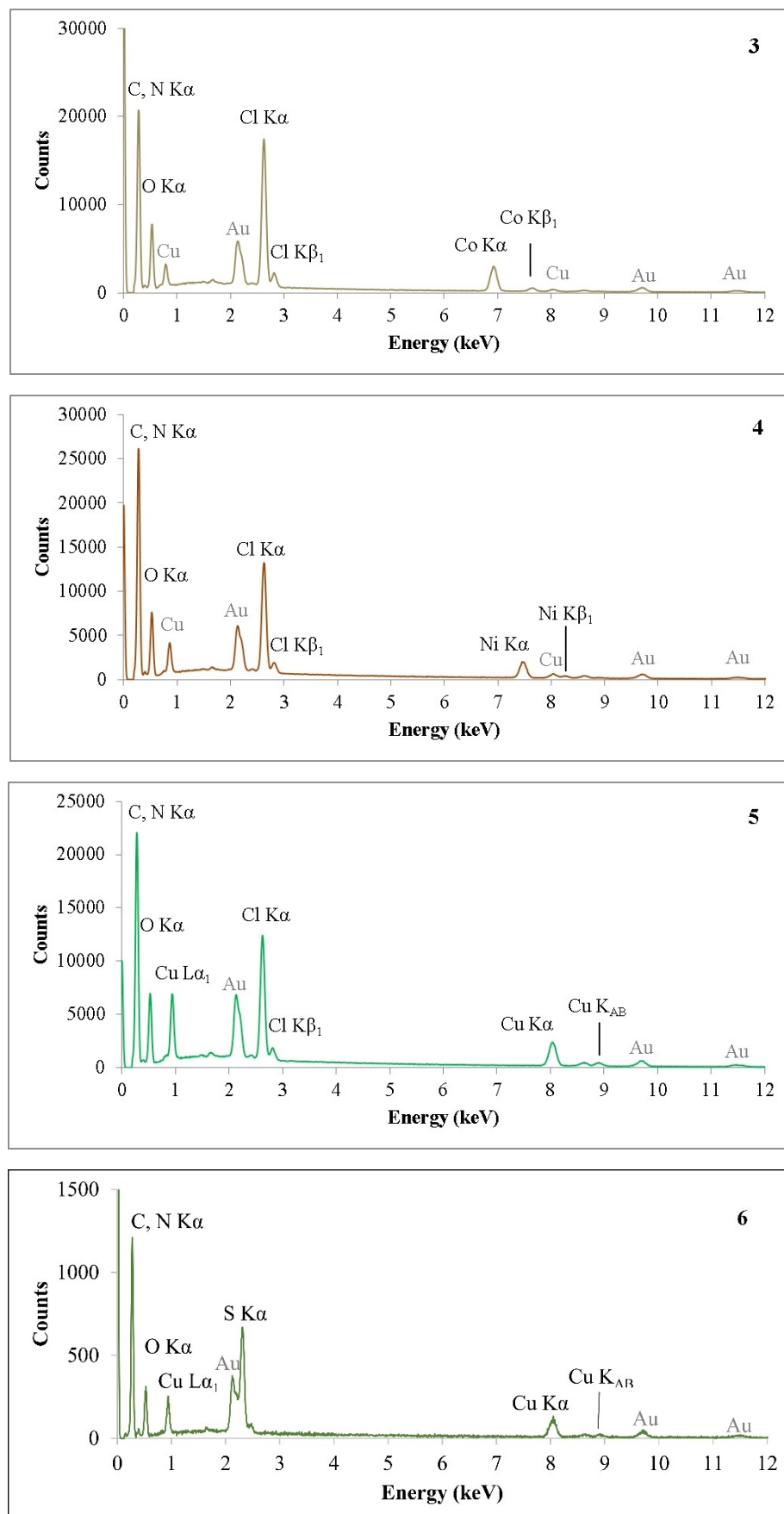


Fig. S8. EDS spectra of compounds **1–6**. Cu (except in **5** and **6**) and Au come from the stub and the metallization process, respectively.

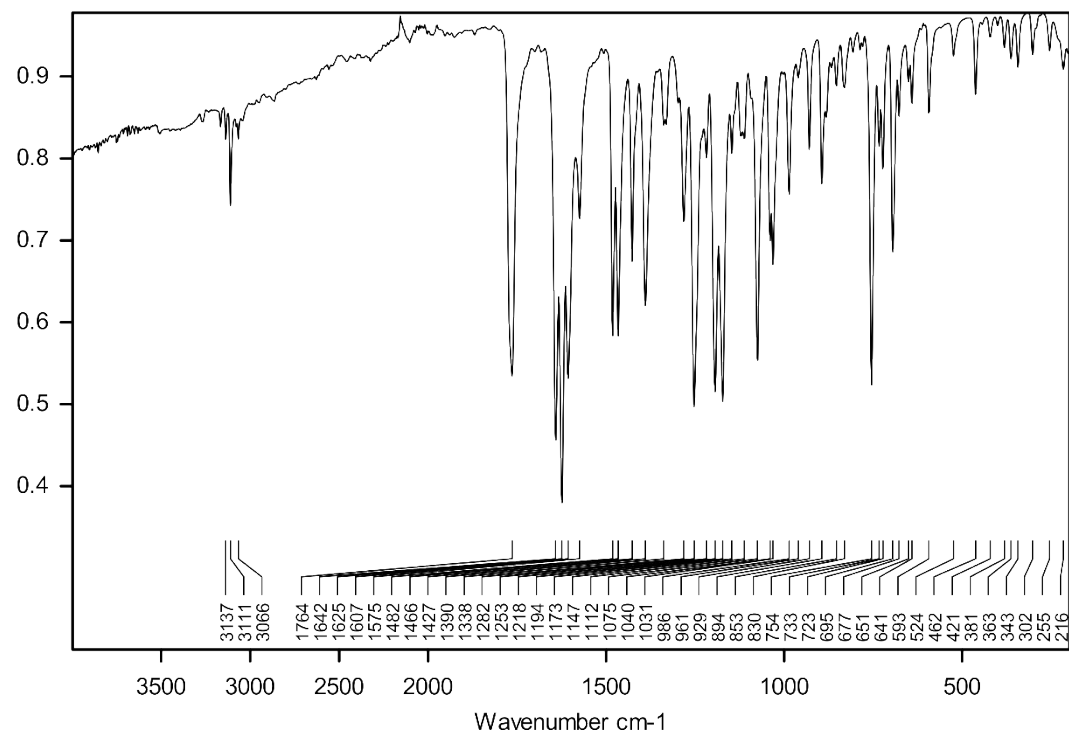


Fig. S9. FTIR spectrum (ATR) of compound 1.

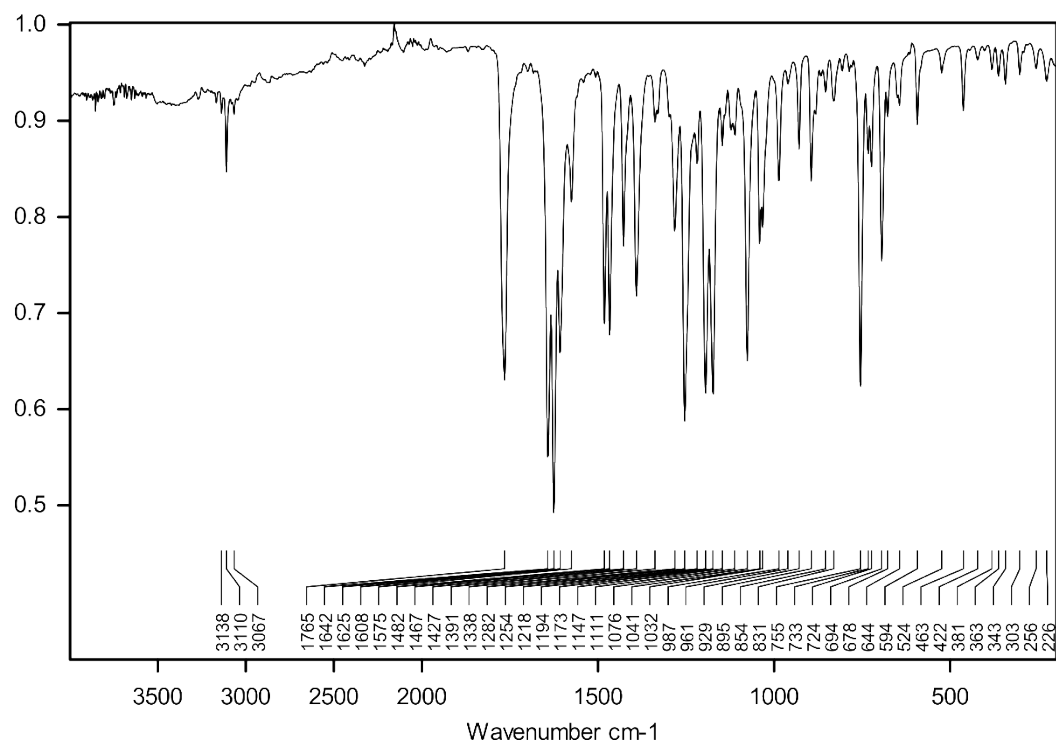


Fig. S10. FTIR spectrum (ATR) of compound 2.

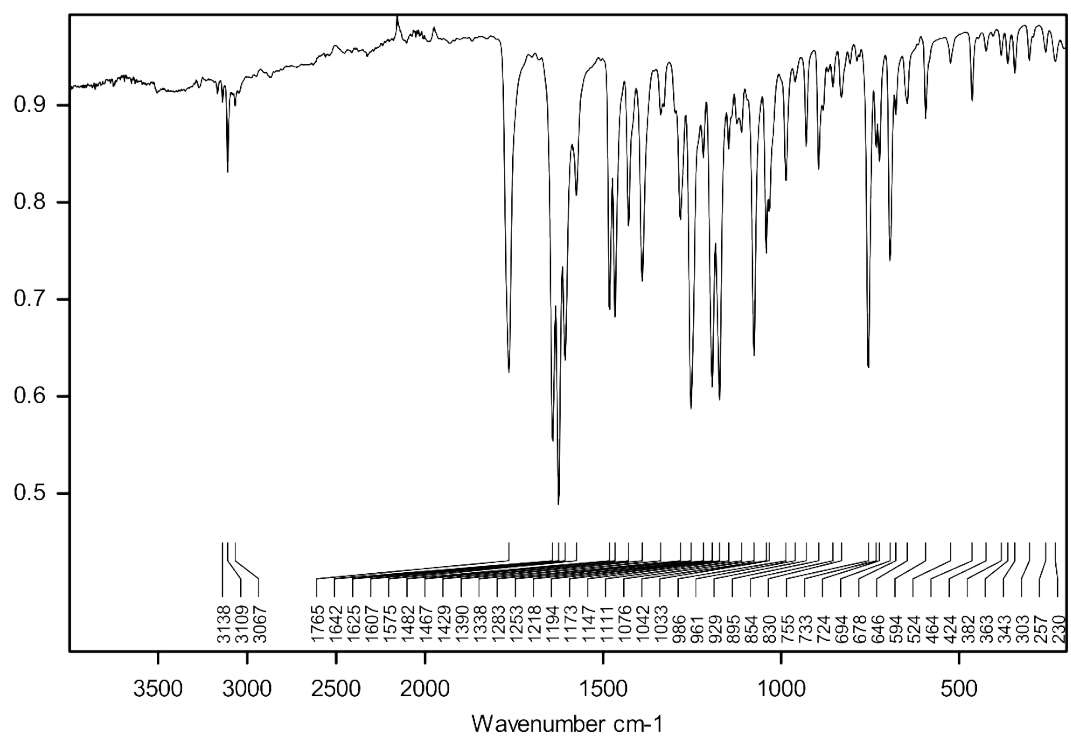


Fig. S11. FTIR spectrum (ATR) of compound 3.

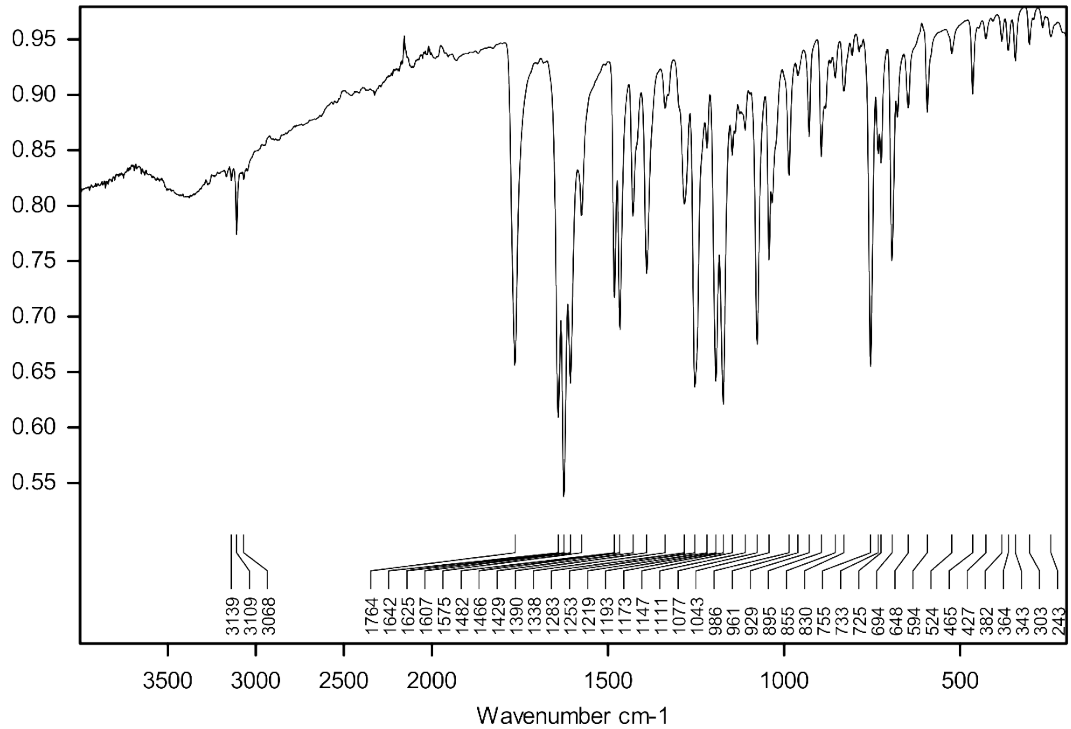


Fig. S12. FTIR spectrum (ATR) of compound 4.

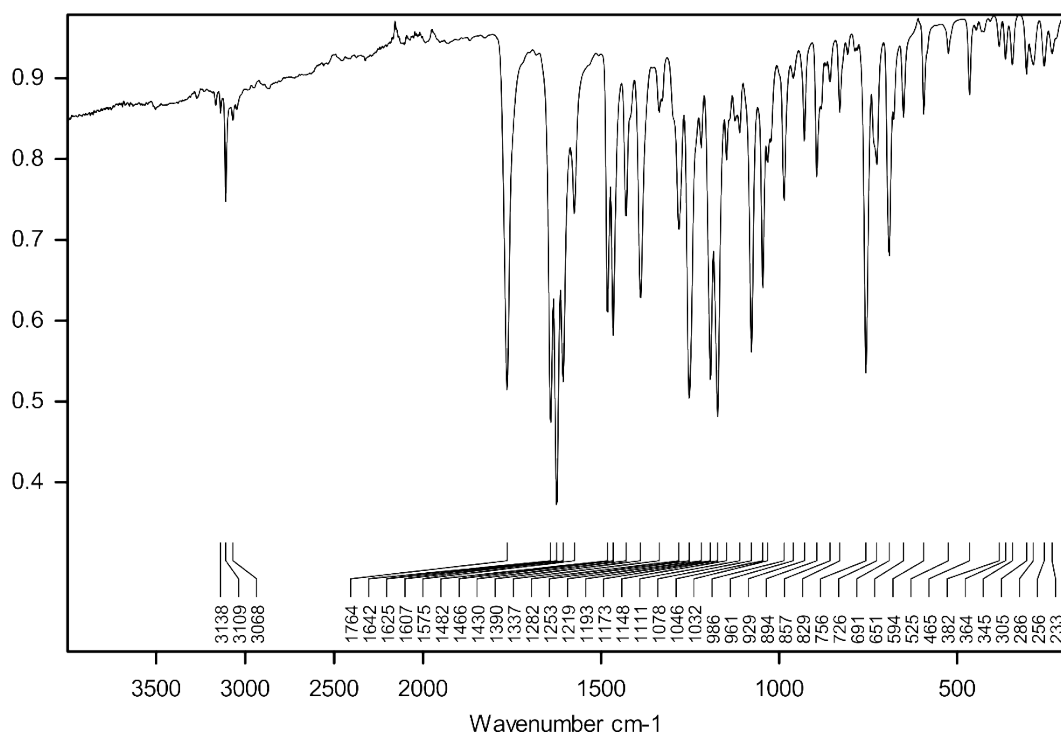


Fig. S13. FTIR spectrum (ATR) of compound 5.

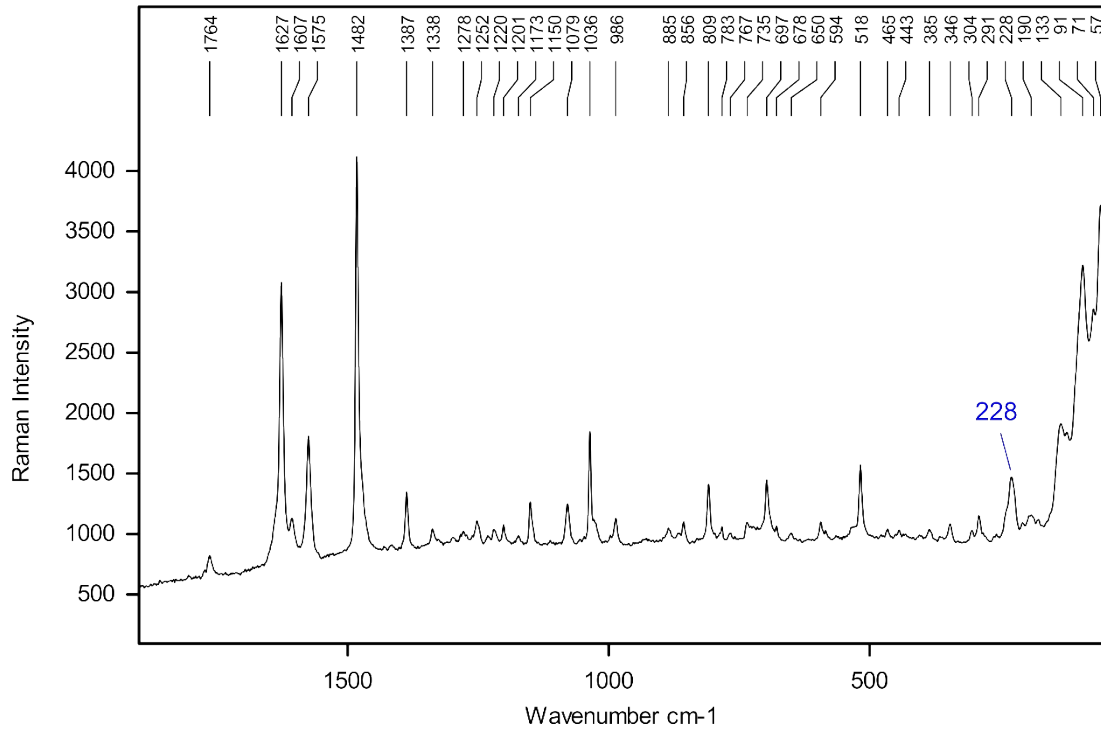


Fig. S14. Raman spectrum of compound 5 in the 1900–50 cm⁻¹ range.

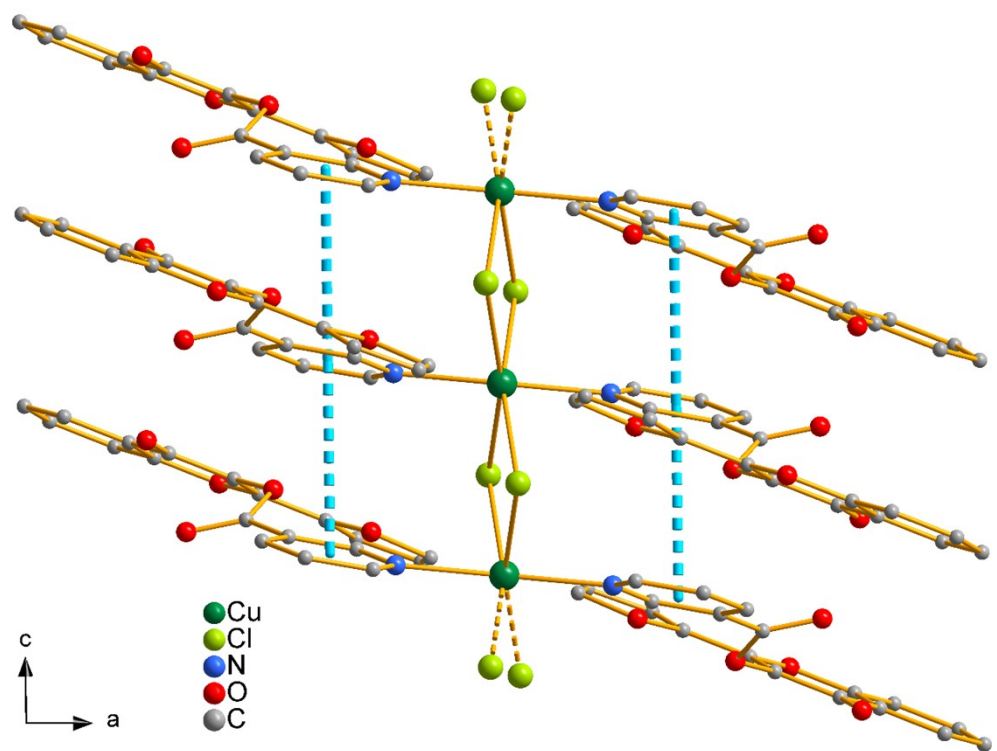


Fig. S15. View of compound **5** in the crystallographic *ac* plane. The blue dashed lines represent the $\pi\cdots\pi$ interactions between the pyridyl rings of the organic ligand.

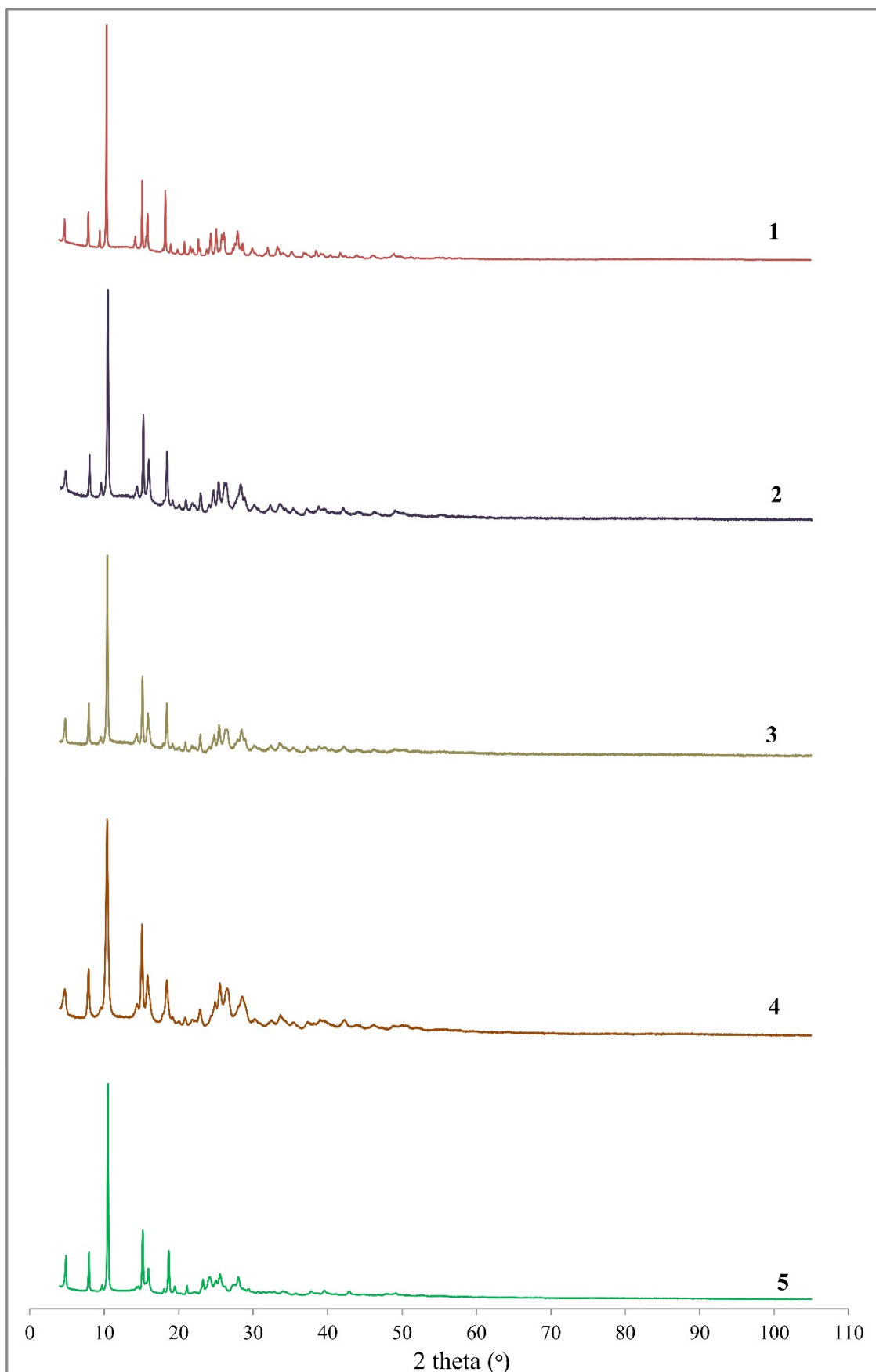


Fig. S16. PXRD diffractograms (7 s per step, step size of 0.02° , Cu-K α) of compounds **1–5**.

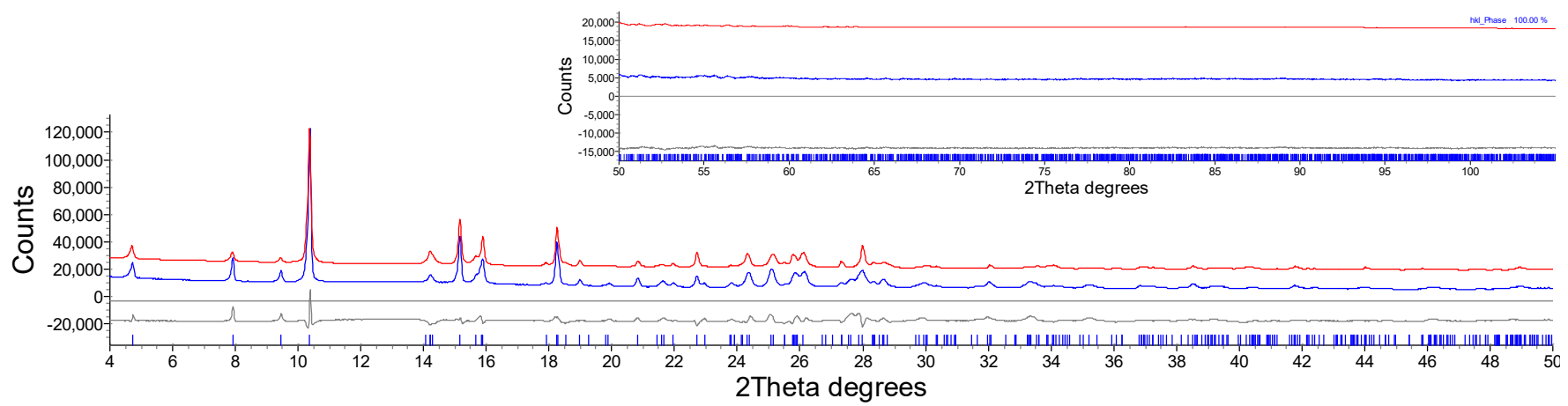


Fig. S17. Final Rietveld refinement plot for the $[\text{MnCl}_2(\text{L})_2]_n$ compound, with difference plot and peak markers at the bottom.

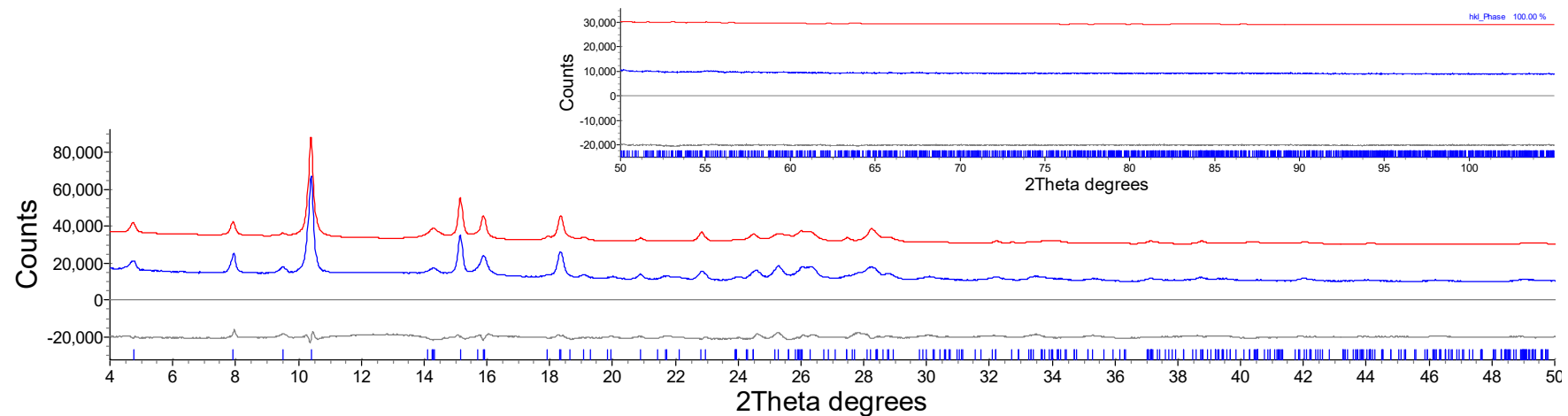


Fig. S18. Final Rietveld refinement plot for the $[\text{FeCl}_2(\text{L})_2]_n$ compound, with difference plot and peak markers at the bottom.

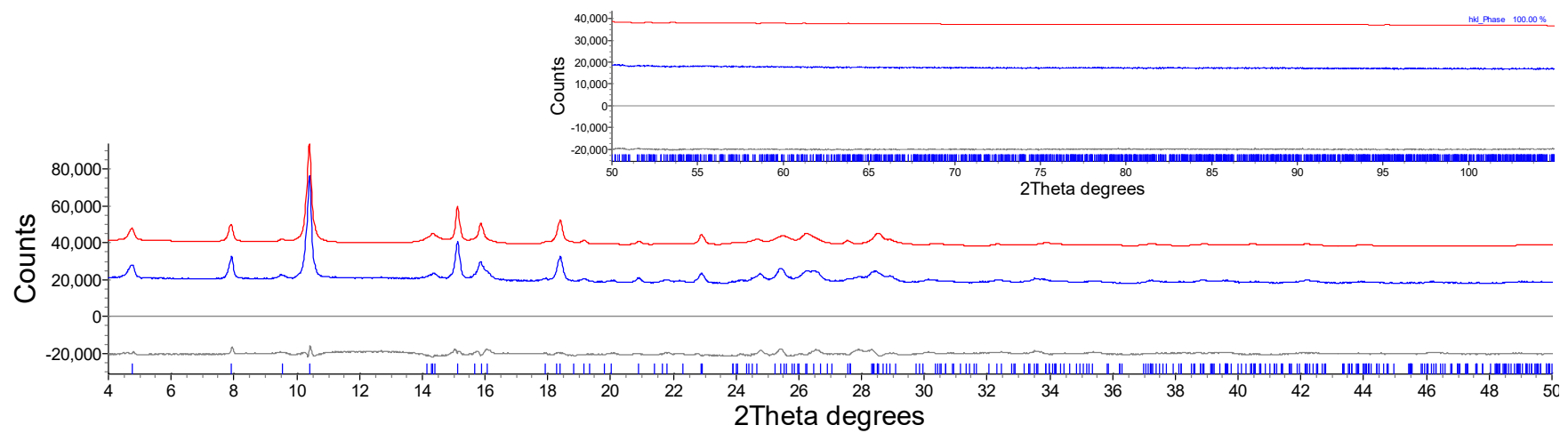


Fig. S19. Final Rietveld refinement plot for the $[\text{CoCl}_2(\text{L})_2]_n$ compound, with difference plot and peak markers at the bottom.

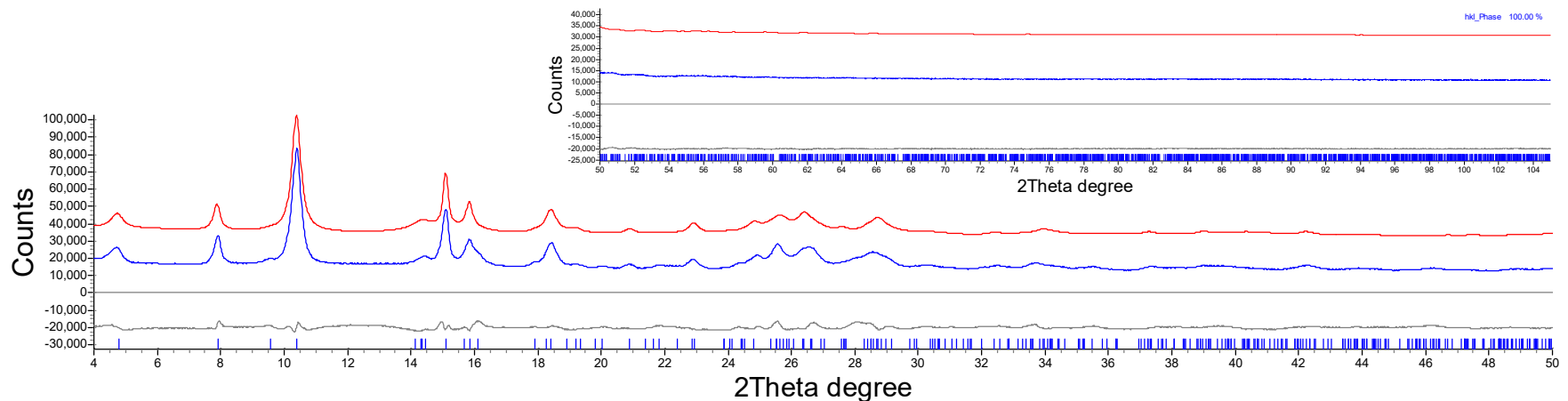


Fig. S20. Final Rietveld refinement plot for the $[\text{NiCl}_2(\text{L})_2]_n$ compound, with difference plot and peak markers at the bottom.

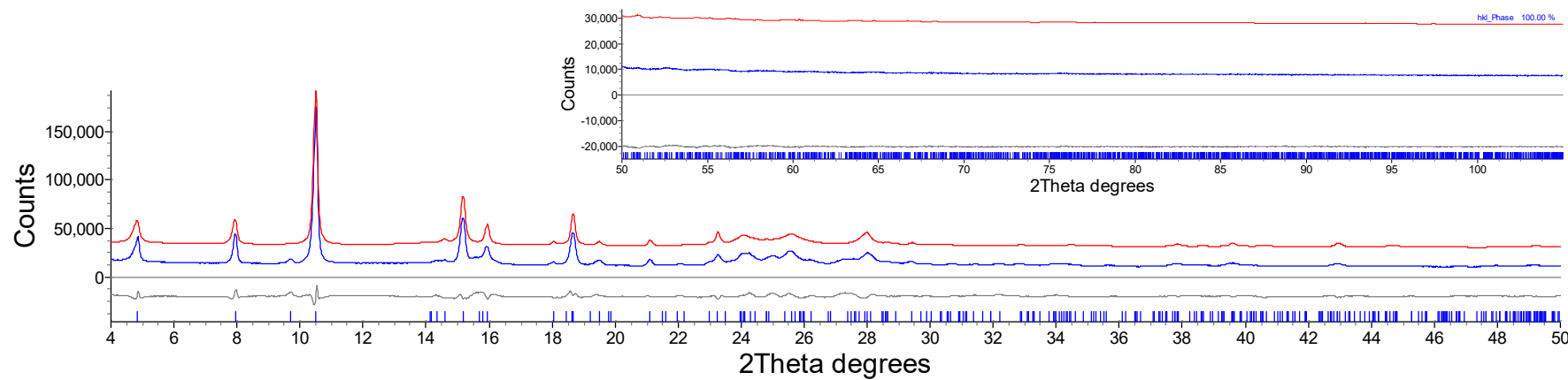


Fig. S21. Final Rietveld refinement plot for the $[\text{CuCl}_2(\text{L})_2]_n$ compound, with difference plot and peak markers at the bottom.

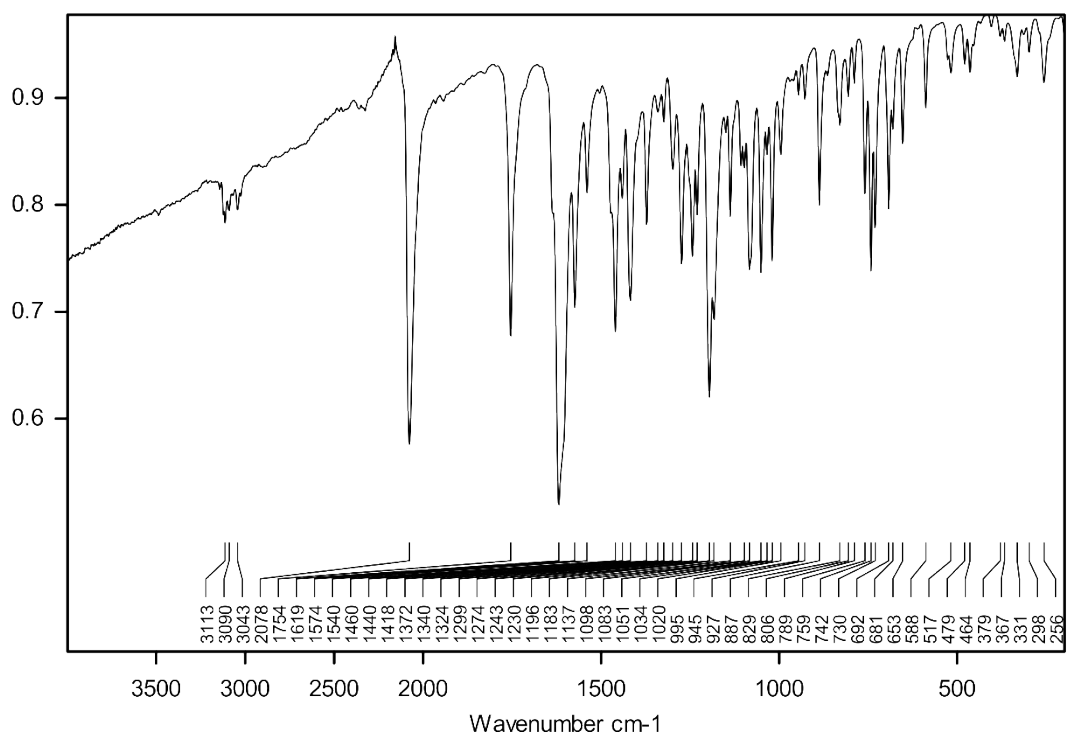


Fig. S22. FTIR spectrum (ATR) of compound **6**.

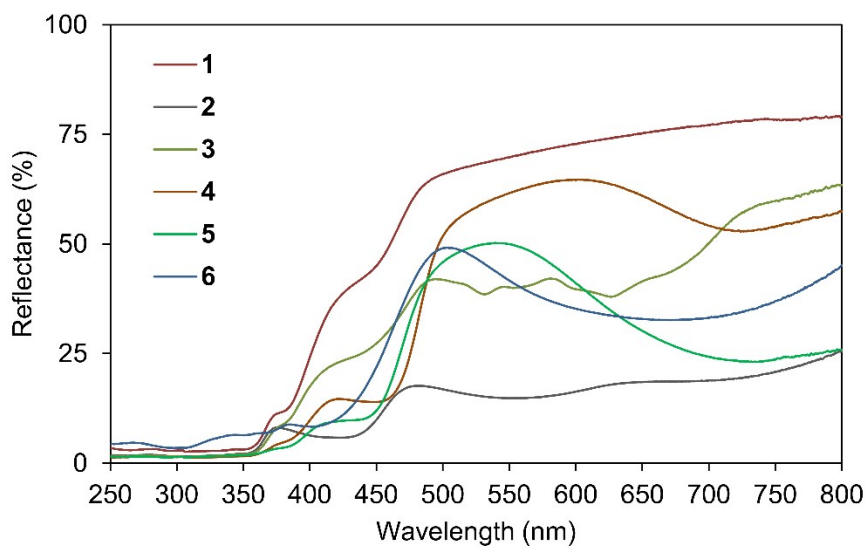
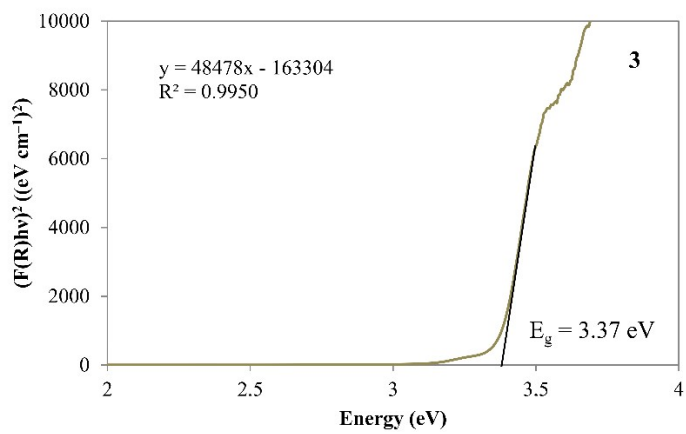
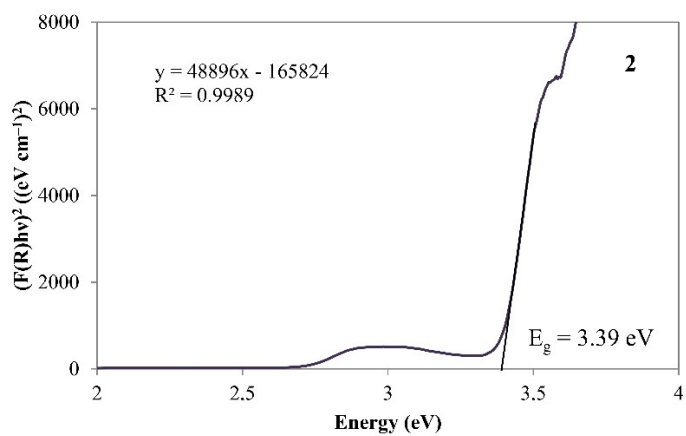
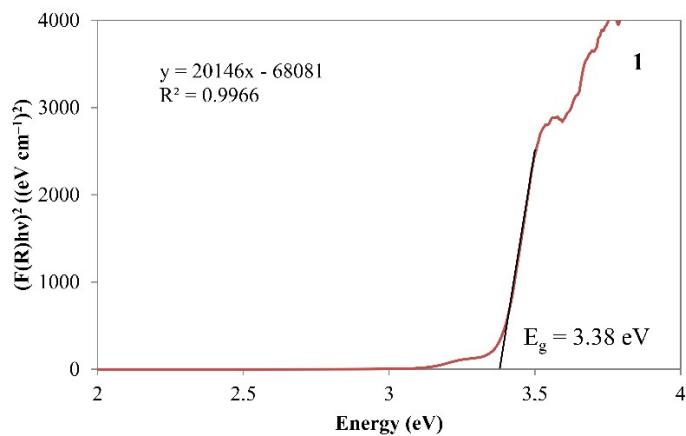
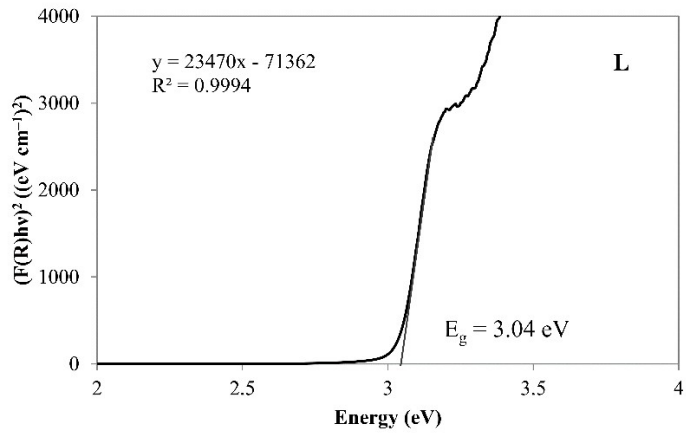


Fig. S23. Diffuse reflectance spectra of compounds **1–6**.



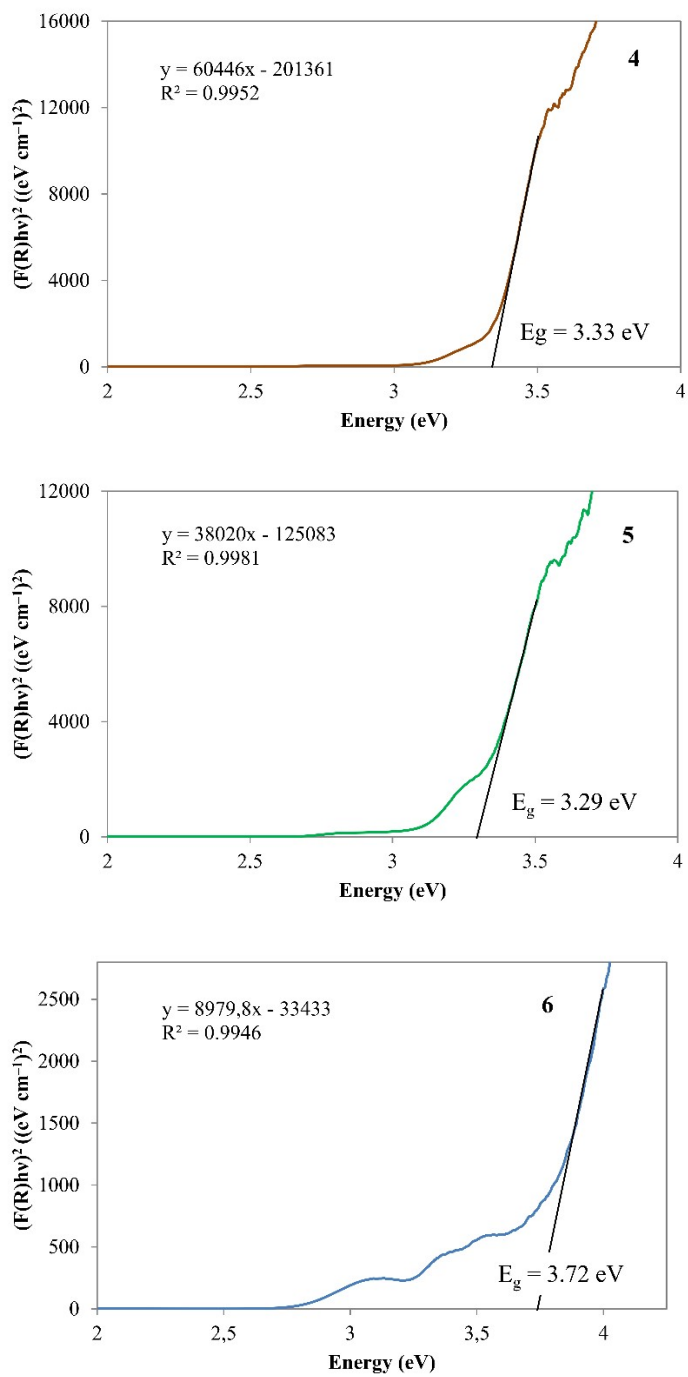


Fig. S24. Tauc plots containing the band gap energies of L and coordination compounds **1–6**.

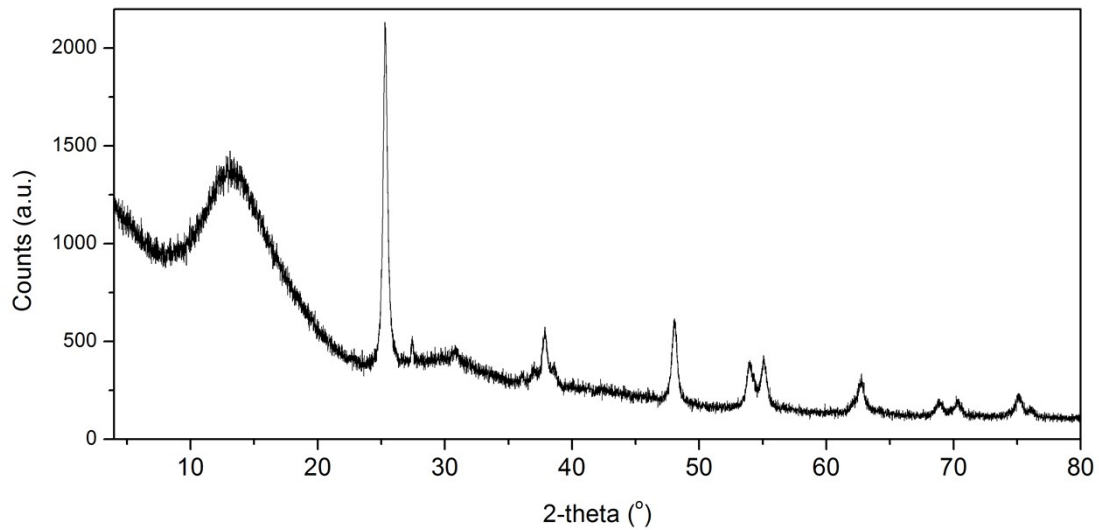


Fig. S25. PXRD diffractogram (0.6 s per step, 0.01° step size, Cu-K α) of mesoporous TiO₂. The mesoporous material contains mainly the anatase phase of TiO₂ (very small amount of rutile phase is present due to the low intensity peaks at 27 and 36 °).

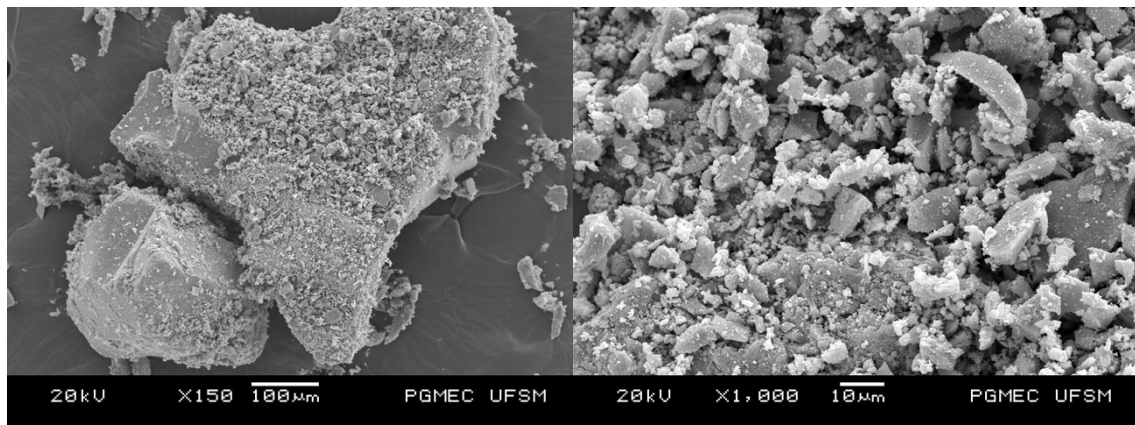


Fig. S26. SEM images of mesoporous TiO₂.

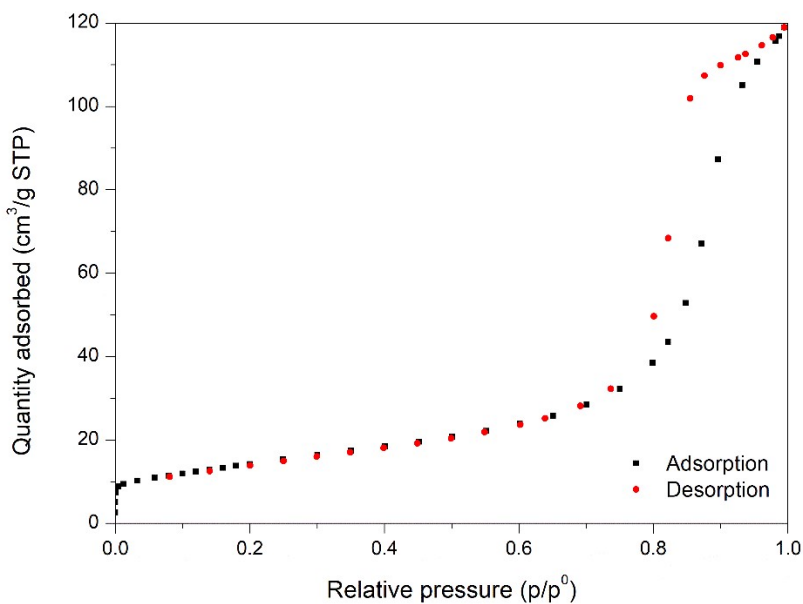


Fig. S27. Nitrogen adsorption/desorption linear isotherm plots of mesoporous TiO_2 .

Table S1. Textural properties of mesoporous TiO_2 :

BET surface area (m^2/g)	Cumulative pore vol. (cm^3/g)	Average pore width (nm)
53.19	0.191	14.37

BET: Brunauer-Emmett-Teller theory [1].

[1]. S. Brunauer, P. H. Emmett and E. Teller, *J. Am. Chem. Soc.* 1938, 60, 309–319.

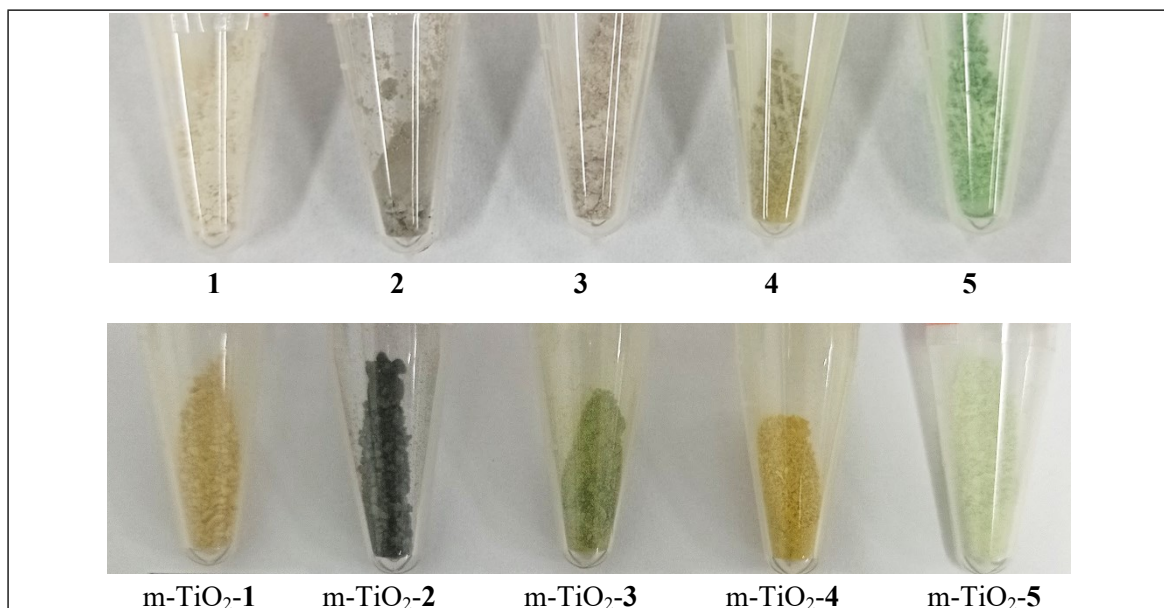
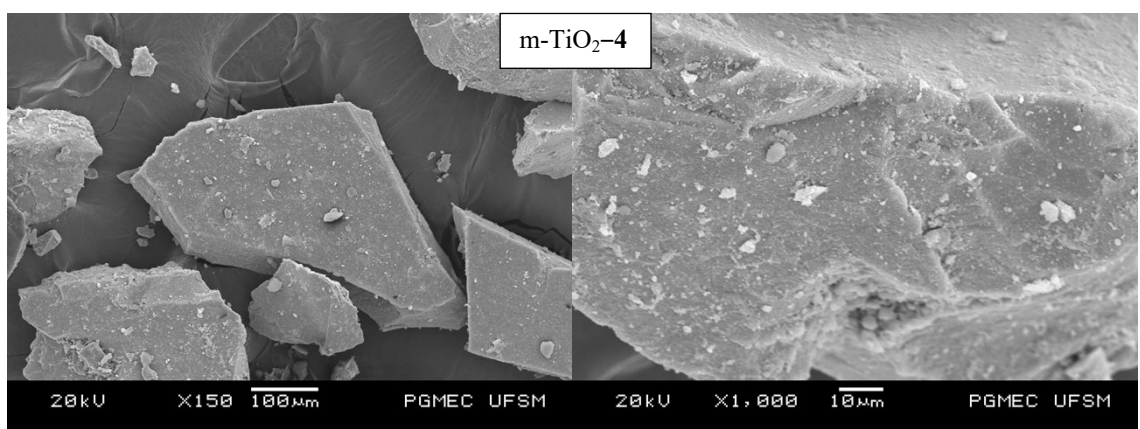
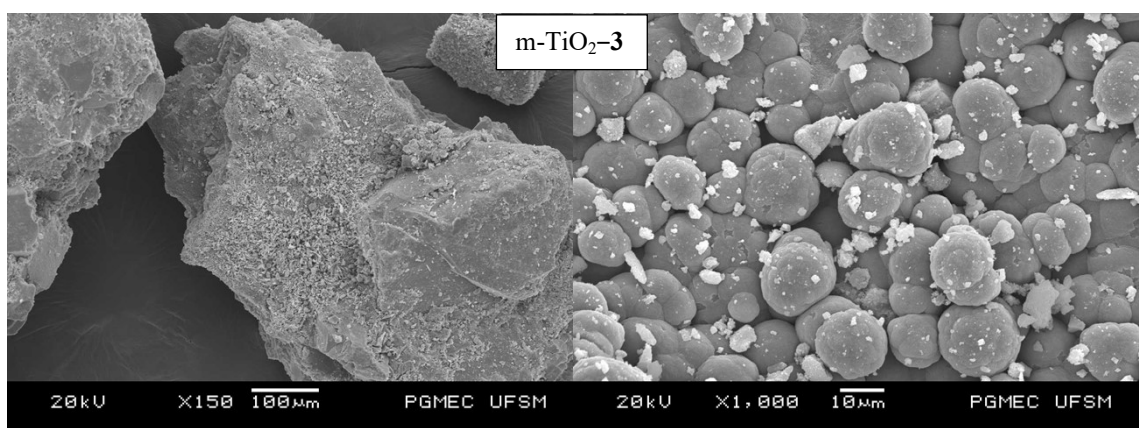
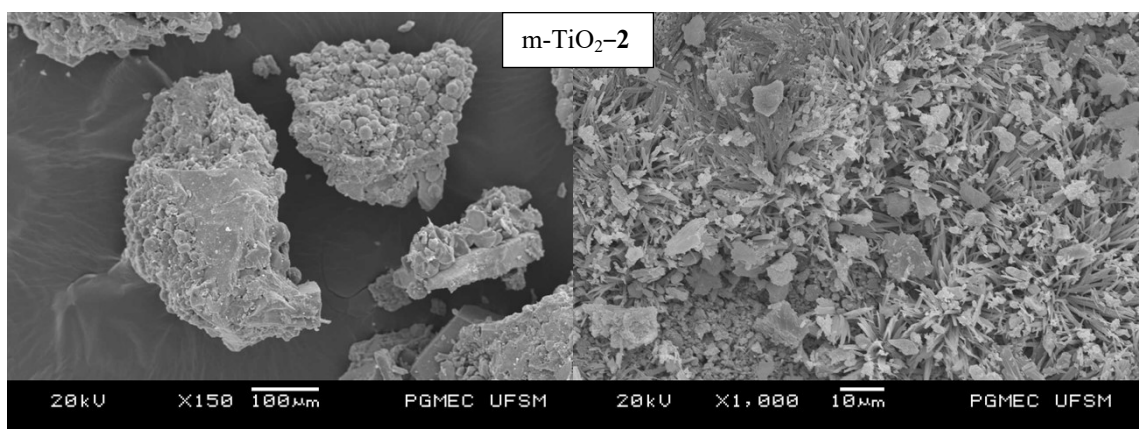
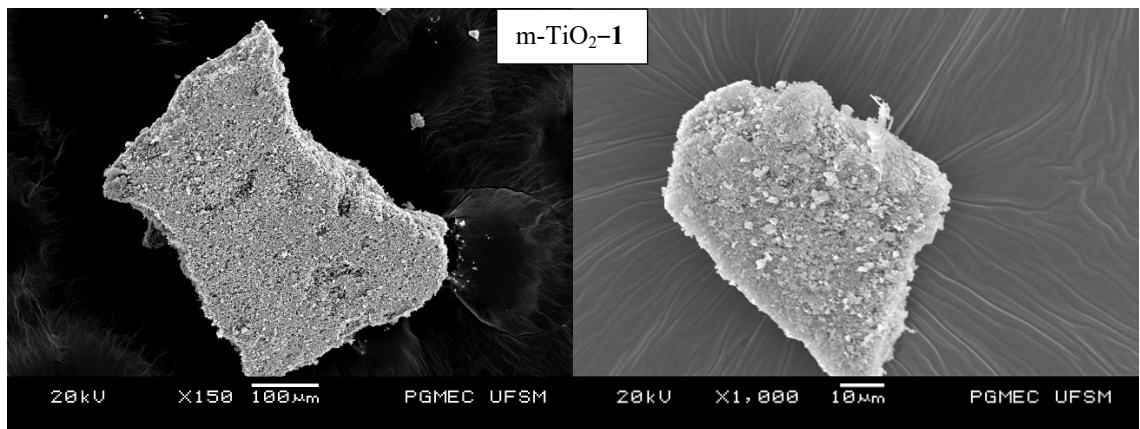


Fig. S28. Color view of compounds **1–5** and their corresponding materials with mesoporous TiO_2 (m- TiO_2).



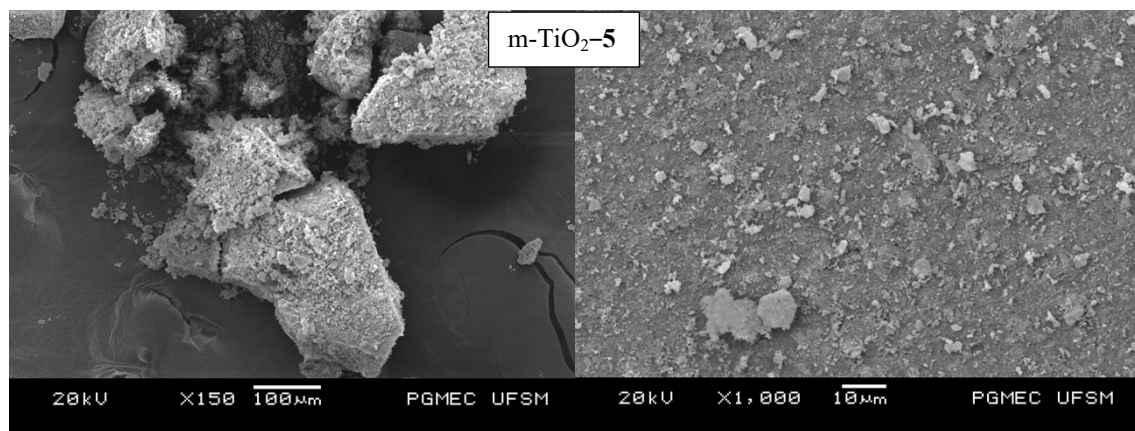
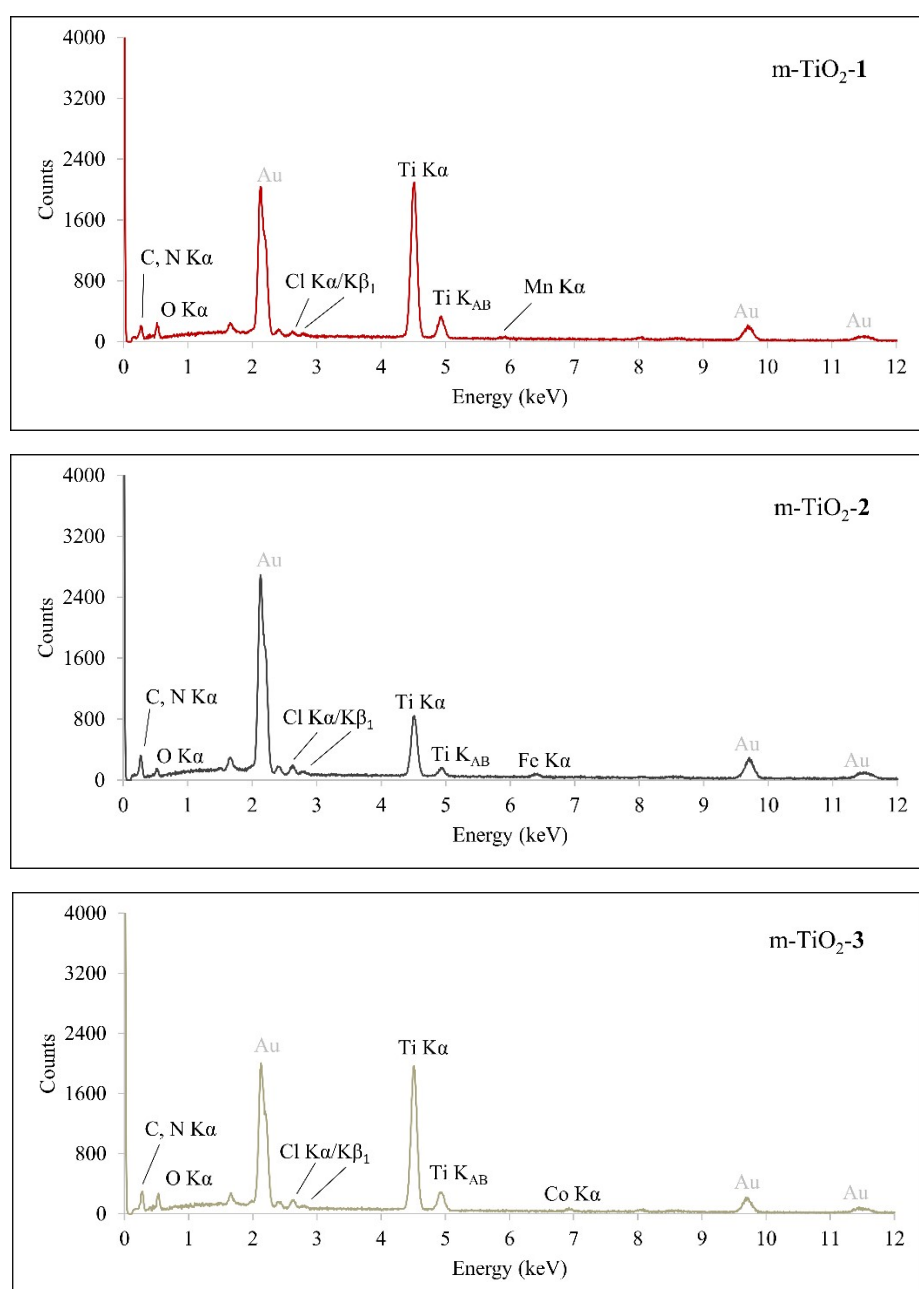


Fig. S29. SEM images of m-TiO₂ containing compounds **1–5**.



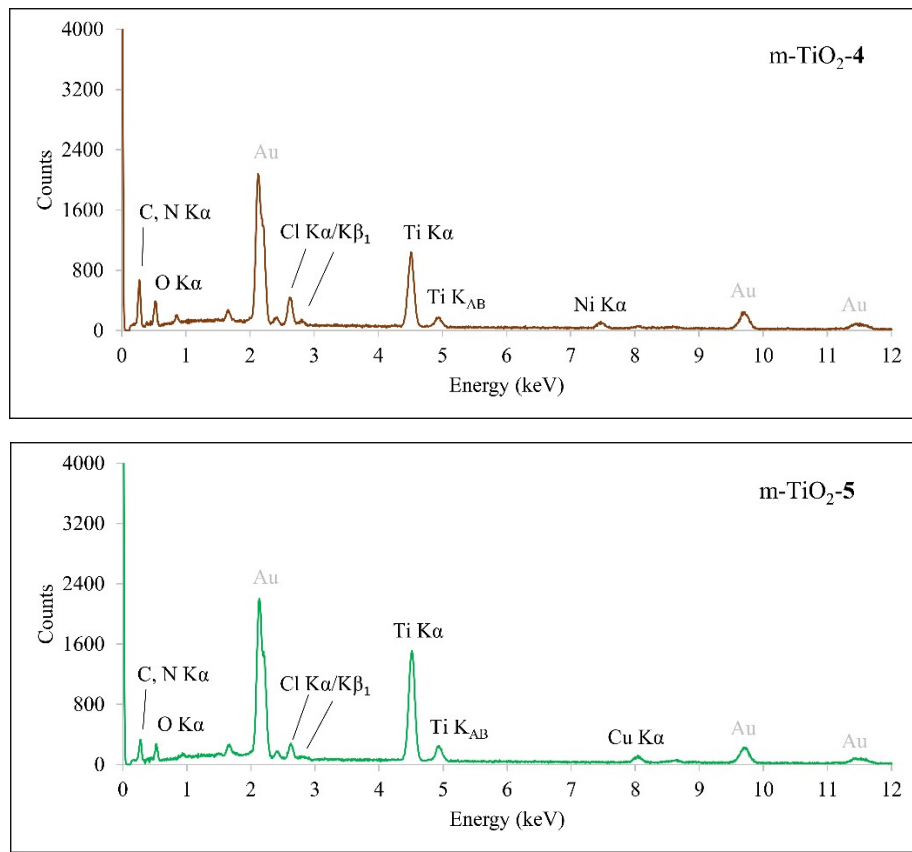


Fig. S30. EDS spectra of $m\text{-TiO}_2$ containing compounds **1–5**. Au comes from the metallization process.

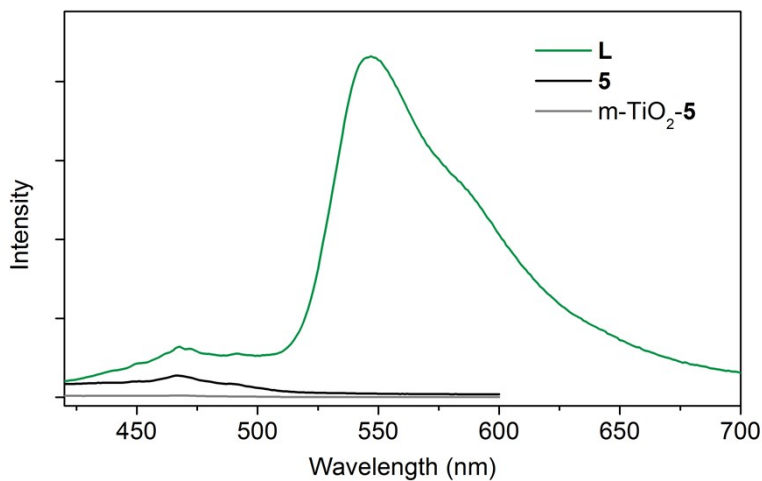


Fig. S31. Solid-state fluorescence spectra of **L**, **5** and $m\text{-TiO}_2\text{-5}$.

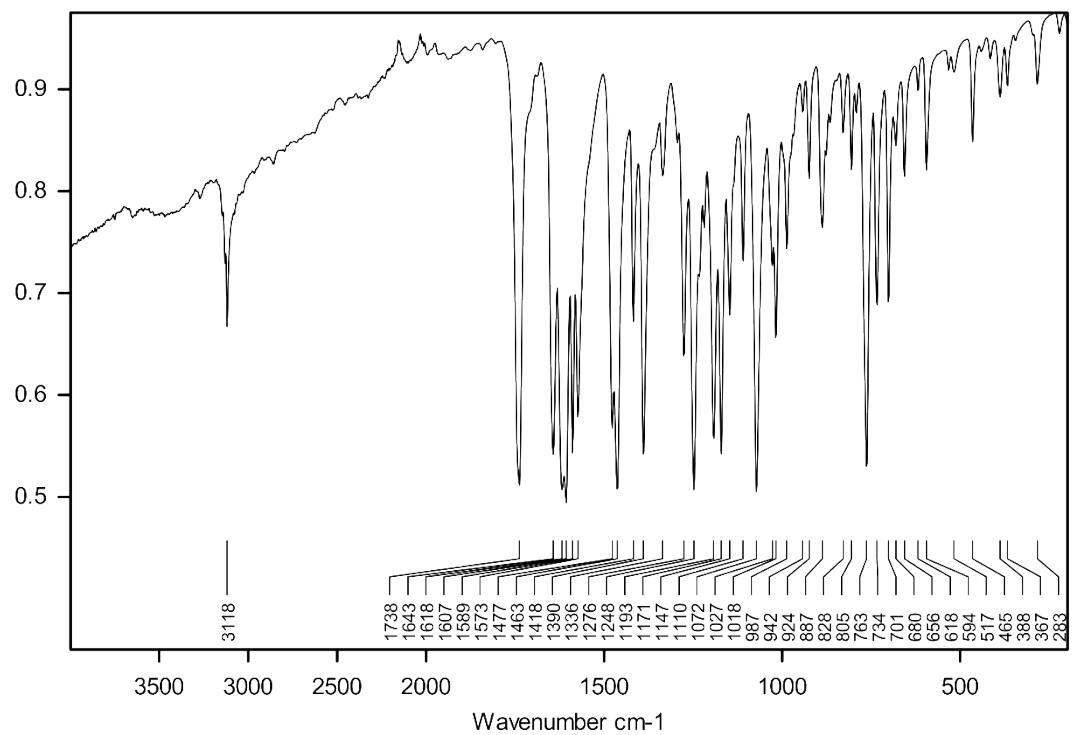


Fig. S32. FT-IR spectrum (ATR mode) of **L**.

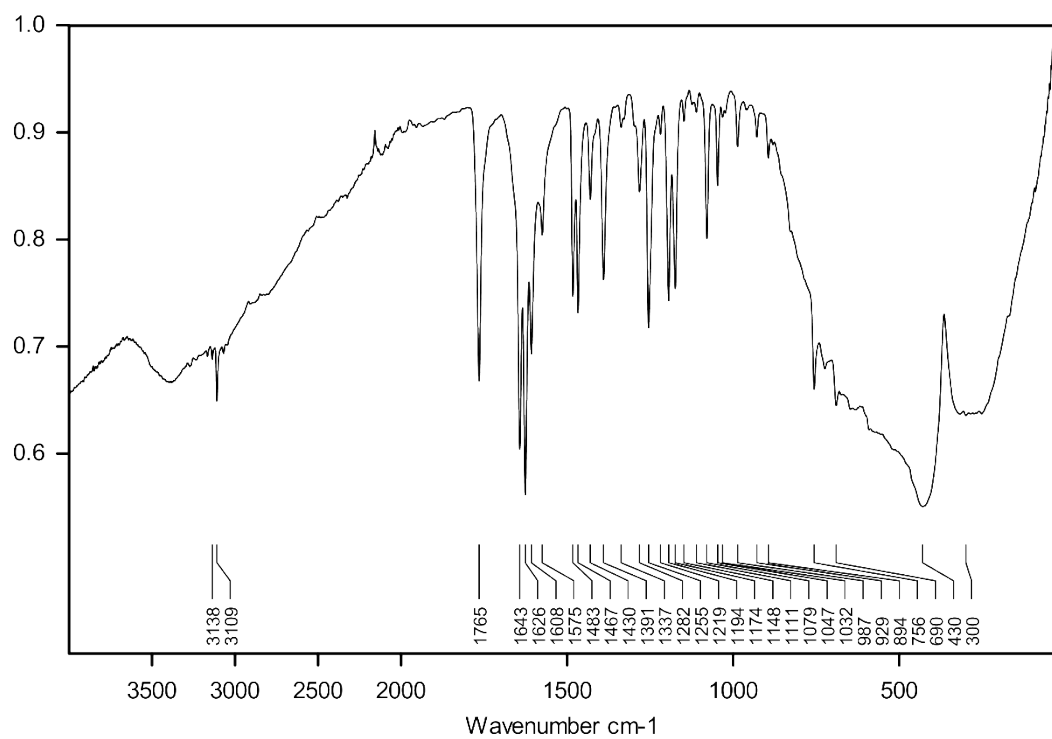


Fig. S33. FT-IR spectrum (ATR mode) of **m-TiO₂-5**.